Aqueous Phase Methanol Reforming Catalyzed by Fe−Cu Alloy Nanoparticles Wrapped on Nitrogen-Doped Graphene

Alberto García-Baldoví, Lu Peng, Andrea Santiago-Portillo, Abdullah M. Asiri, Ana Primo,* and Hermenegildo García*

ACCESS | 📊 Metrics & More | 📄 Article Recommendations | 🆂�🅸 Supporting Information

ABSTRACT: Small Fe−Cu nanoparticles (NPs) (about 1 nm) supported at a high loading (over 10 wt %) on N-doped graphitic carbon have been prepared in a single pyrolytic step from chitosan adsorbing Cu^{2+} and Fe^{2+} salts. The presence of N atoms appears to be crucial in the formation of small-sized metallic NPs. Interactions between Fe and Cu are reflected by a shift in the binding energy to higher (Fe) or lower (Cu) values and by H_2 thermo-programmed reduction measurements, showing a new reduction peak at intermediate temperature (375 °C) between that of Cu (175 °C) and that of Fe (450 °C). Fe−Cu NPs embedded within the N-doped graphitic carbon matrix are extremely active (TOF 315 h^{-1}) and selective (no CO detected) catalysts for methanol reforming in the aqueous phase with stoichiometric H_2O amounts to H_2 and CO_2. The results achieved with Fe−Cu compare favorably with those reported in the literature for catalysts based on Pt, Pd, or Ru.

KEYWORDS: *heterogeneous catalysis, aqueous phase reforming, hydrogen from methanol, liquid hydrogen organic carrier, N-doped graphitic carbon as a support*
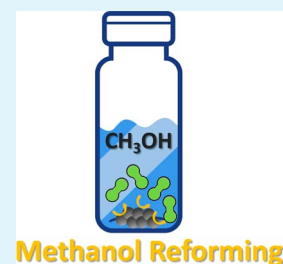
■ INTRODUCTION

In the context of the shift from fossil fuels to decarbonized energy, hydrogen is among the most promising alternative energy vector for transportation.[1] The main problem to implement hydrogen as automotive fuel is its low volumetric energy density, when employed as compressed gas.[2] Among the various strategies to load hydrogen for transportation, one of the most appealing approaches consists in the use of a liquid organic compound that by decomposition gives rise *upon-demand* to *on-board* hydrogen. Various organic compounds have been proposed as liquid organic hydrogen carriers (LOHCs), including hydrogenated aromatic compounds and heterocycles.[3] Among these LOHCs, one that has attracted considerable attention due to its high hydrogen loading is methanol.[4] Besides self-decomposition, the reaction of methanol with water (methanol reforming) gives an additional hydrogen molecule from water and forms CO_2 (Scheme 1). When methanol is obtained from CO_2, the footprint of the methanol formation—methanol reforming process is neutral, thus, meeting the requirement of decarbonized energy. The

combined methanol formation/methanol decomposition cycle acts as a liquid hydrogen carrier system.

Hydrogen release from CH_3OH can be performed by reacting methanol and water in the liquid phase (aqueous phase methanol reforming). The process requires of a catalyst to take place under mild conditions at adequate rates. Compared to other LOHCs, the aqueous phase reforming process has the advantage of higher hydrogen loading, no need to recover the hydrogen-depleted products to be recycled and water compatibility, making the whole process more convenient from the environmental point of view.

Similar to formic acid decomposition,[5] most of the catalysts reported so far for aqueous phase methanol reforming are based on noble or semi-noble metals, such as Pt and Ru.[6] Catalysts based on non-noble metals mostly contain Ni and Ni with dopant elements (Ce, Zr, and La) supported on metal oxides such as alumina and zirconia.[7] In more recent years, graphene has become also among the preferred supports for metal nanoparticles (NPs) due mainly to its large surface area and the strong metal−graphene interaction that stabilizes metal NP size under reaction conditions and tunes electron density at the metal NPs.[8] The presence of defects and doping on graphene can generally play a positive role in not only
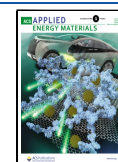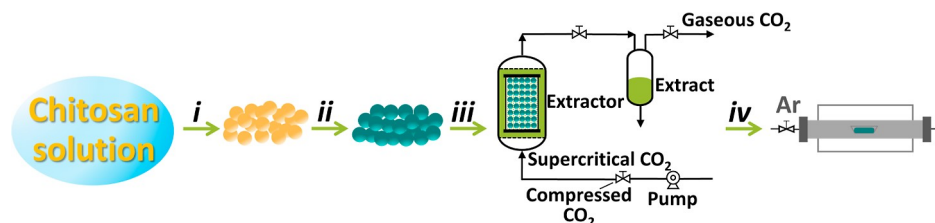
Scheme 1. Catalytic Methanol Reforming Releasing H₂

$$CH_3OH + H_2O \longrightarrow 3H_2 + CO_2$$

9173
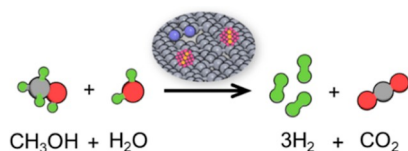
Scheme 2. Preparation Procedure of the Fe−Cu@(N)C Samples under Study[a]

[a](i) Precipitation in NaOH solution of chitosan spheres; (ii) water/ethanol exchanges and subsequent metal salt adsorption in ethanol; (iii) supercritical CO_2 drying; and (iv) pyrolysis in a horizontal electrical oven under an Ar flow.

Table 1. Main Analytical and Physicochemical Parameters of the Fe−Cu@(N)C Samples under Study

sample no.	Cu (wt %)[a]	Fe (wt %)[a]	total Cu + Fe (wt %)[a]	molar ratio (Cu/Fe)	N (wt %)[b]	C (wt %)[b]	average particle size (nm)[c]
1	15.1		15.1		4.3	71.9	1.4 ± 0.3 (5.9)
2		13.0	13.0		3.2	76.0	1.1 ± 0.3 (6.5)
3	8.2	2.5	10.7	2.9	4.2	69.7	1.1 ± 0.2 (5.4)
4	3.4	14.6	18.0	0.1	2.3	74.2	1.3 ± 0.4 (6.2)
5	12.2	6.2	18.4	1.7			>100 (89.7)

[a]Determined by inductively coupled plasma-atomic emission spectroscopy analysis after dissolving the metals in *aqua regia*. [b]It is assumed that the difference to 100% is residual oxygen. [c]Determined from the DF-TEM images or from XRD (values in brackets).

increasing the metal−graphene interaction strength but also cooperating to the catalysis by providing additional sites to adsorb and activate substrates and reagents.[9]

Herein, the catalytic activity of small Fe−Cu NPs (1−2 nm) wrapped on N-doped graphene to promote the aqueous phase methanol reforming is presented. The role of nitrogen on graphene allowing the formation of highly active small metal NPs as well as the benefits of metal combination by tuning the electron density transfer of the active sites will be commented. It is worth noting that while different Cu alloys have been reported in catalysis, the combination of Cu and Fe has remained almost unexplored.[10] It will be shown that the combination Fe−Cu exhibits an activity for aqueous methanol reforming higher than an analogous catalyst based on the much more widely studied Cu−Zn combination, thus surpassing the current benchmark catalyst in the area.

RESULTS AND DISCUSSION

The samples under study were prepared by impregnation of chitosan alcogels with the corresponding Cu and Fe salts dissolved in ethanol in various Cu/Fe atomic proportions (Table S1 in Supporting Information). After metal adsorption, the resulting metal containing chitosan microspheres of submillimetric diameter were dried with supercritical CO_2. This procedure is known to render highly porous, high-surface area chitosan powders.[11] This is due to the loose packing of chitosan fibrils when the sample is dried in supercritical CO_2, by avoiding strong hydrogen bonding.[12] The final step in the synthesis consists in the pyrolysis at 900 °C under an inert atmosphere, converting chitosan into N-doped defective graphene.[13] At the same time, due to the reducing conditions of the pyrolysis, the Cu^{2+} and Fe^{2+} ions are simultaneously reduced to their metallic state forming fine NPs, similar to what has been reported in the literature and denoted as

carbochemical metal reduction.[14] The synthesis process is illustrated in Scheme 2. Table 1 lists the samples of Cu, Fe, and their combinations under study. As it can be seen in this Table 1, two of the samples only contain Cu and Fe, while other three are combinations of Fe−Cu metal in different Cu/Fe atomic ratios from about 2.9 to 0.1.

The samples prepared were aimed at having similar total Cu + Fe metal loadings, varying the Cu/Fe atomic ratio. However, unavoidable variations in the total metal content due to the differences in metal adsorption and variations in the exact mass loss during pyrolysis [steps (ii) and (iv) in Scheme 2] were measured by chemical analysis. In any case, the average particle size, which is a relevant parameter influencing the catalytic activity, was similar in all cases with an average diameter slightly above 1 nm. Table 1 also includes a similar Fe−Cu sample prepared using alginate instead of chitosan (sample **5**). Alginate is a polysaccharide of guluronic and mannuronic acids, and it does not contain N in its composition. In comparison, chitosan is the homopolymer of glucosylamine and has about 8 wt % N in its composition. Part of this N content remains in the resulting graphene, as confirmed by combustion chemical analysis (see Table 1) and X-ray photoelectron spectroscopy (XPS). The set of catalysts was prepared with the purpose of comparing the catalytic behavior of the samples depending on the presence of nitrogen atoms as the dopant element. Importantly, a salient observation was that the particle size for the samples containing a defective graphitic carbon matrix lacking nitrogen was considerably much larger about 100 nm than the size of the Fe−Cu NPs embedded within N-doped graphitic carbon matrix that are about 1 nm.

X-ray diffraction (XRD) patterns indicate that after pyrolysis, the materials are constituted by independent metallic Cu (fcc) and Fe (bcc) phases with no real random alloy since there are no obvious shifts in the position of the most important XRD peaks of both pure metals. Figure 1 illustrates
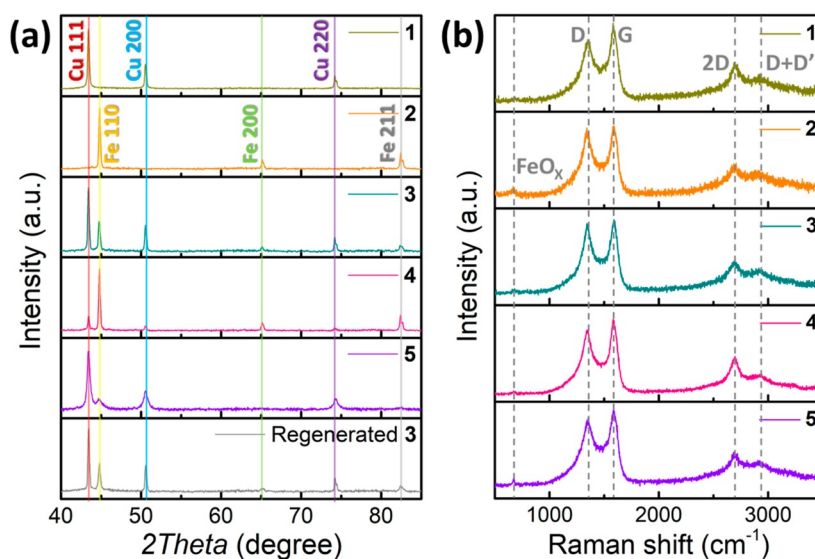
Figure 1. XRD patterns [Fe] and Raman spectra (b) of catalysts **1** to **5**. Part (a) also includes the diffraction pattern of sample **3** after being used as a catalyst five times.
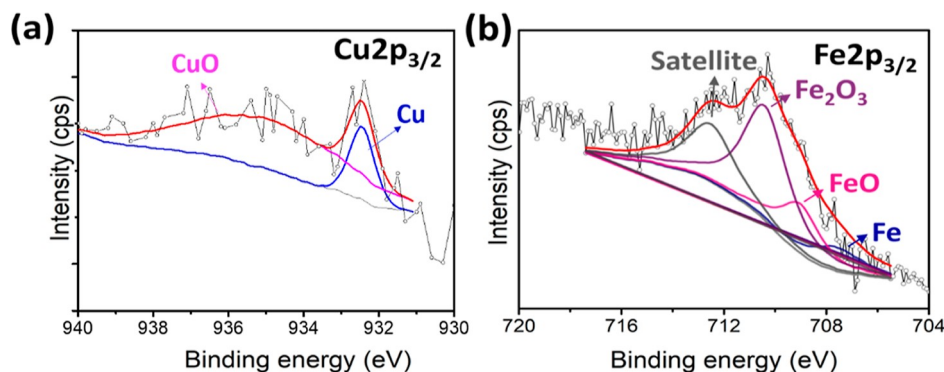
Figure 2. High-resolution XPS Cu $2p_{3/2}$ (a) and Fe $2p_{3/2}$ (b) peaks of catalyst **3** and the corresponding best fitting to single components.

the metallic phase and the lack of random alloying of the samples under study. An average particle size was determined from the peak width by applying the Scherrer equation. The results are given in Table 1.

The graphitic nature of the carbon matrix formed in the pyrolysis was confirmed by Raman spectroscopy (Figure 1) where the three characteristic vibration peaks at 2750, 1590, and 1350 cm^{-1} corresponding to 2D, G and D bands recorded in graphitic carbons were observed. Interestingly, the presence of a weak band in the low-frequency spectra zone about 668 cm^{-1}, mainly observed for the samples containing Fe, would indicate the presence of metal oxides (particularly FeO$_x$). It is proposed that this MO$_x$ would correspond to a thin outermost external layer of metal NPs due to the exposure to ambient oxygen. However, the weak intensity of this Raman band, together with the XRD patterns corresponding to metallic elements, indicates that this MO$_x$ oxide overlayer should be a minor proportion of the metallic elements.

In spite that Cu and Fe are in separate phases, they should be in close proximity embedded within the graphitic carbon matrix, probably establishing an interaction. The interaction between the Cu and Fe is clearly revealed by XPS analysis. Figure 2 shows the XPS the Cu 2p and Fe 2p peaks of sample **3**, while Tables S2 and S3 in the Supporting Information collects the XPS data for all the samples under study. This

surface technique shows the presence of the expected peaks corresponding to C 1s, O 1s, and N 1s with a distribution of families in agreement with the previous reports for N-doped-defective graphenes derived from chitosan and their relative proportions (see Figure S1 and Table S2).[13,15] For Cu and Fe, deconvolution of the experimental Cu 2p and Fe 2p peaks reveals the presence of these metals in various oxidation states (see Figure 2). The presence of these oxidation states is common in metal NPs and corresponds to metal atoms at the most external layers of metal NPs exposed to the ambient as it has been reported for related metal NPs on the same graphitic carbon matrix.[16,17] Thus, these XPS data agree with the previously commented Raman spectra. However, oxidation states higher than the metallic state should be minor according to XRD patterns that correspond to Cu and Fe metal. Importantly, the binding energy values for the Cu^0 component increase from 930.8 eV corresponding to the Cu metal in sample **1** (only Cu) to 931.6 eV when Cu and Fe are simultaneously present in sample **3**. On the contrary, the major Fe component (Fe^{III}) decreases from the 711.3 eV in sample **2** (only Fe) to 710.4 eV in sample **3**, in which there should be a Cu−Fe interaction. This comparison of XPS of samples **1** and **2** with the other samples provides quantitative data on the Cu−Fe interaction when the two metals are present.
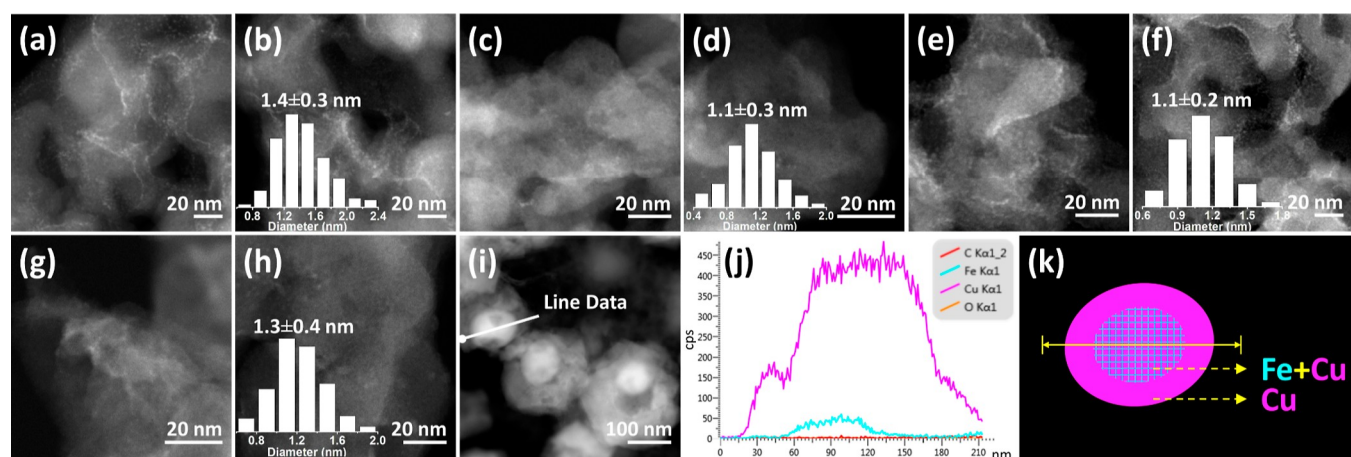
Figure 3. DF-TEM images (a−i) of samples **1**−**5** [(a,b) sample **1**; (c,d) sample **2**; (e,f,) sample **3**; (g,h) sample **4**; (i) sample **5**]. (j) Element distribution by EDS across the white line of frame (i); and (k) schematic illustration of core−shell structure according to EDS. Insets: histograms of particle size distribution.

The morphology at the submicrometric level of the graphitic carbon matrix resulting after the pyrolysis was analyzed by field emission scanning electron microscopy (FESEM) images (Figure S2). These images show identical morphologies for samples **1** to **4**, regardless of the metal composition. The graphitic carbon matrix appears as a spongy, highly porous, coral-like material. Similar morphologies have been previously observed for this type of graphitic carbon obtained by pyrolysis of natural polysaccharides.[11] This structure of graphitic carbons is inherited from the polysaccharide precursor after the supercritical CO_2 drying that is known to impart high porosity and high-surface area due to the absence of strong packing of the linear polysaccharide fibrils.[18] Importantly, the presence of metal NPs could not be observed in these images due to their very small size and the insufficient resolution of the FESEM technique.

The presence of Cu and Fe NPs on the carbon matrix and their average particle size for samples **1**−**4** could be determined by transmission electron microscopy in dark field (DF-TEM). Figure 3 shows representative images taken from these samples **1** to **4**. As it can be seen there, the presence of a uniform distribution of small metal NPs was observed in these images from the bright contrast of the image background, without the presence of defined large NPs. Although the metal was dispersed on all the carbon matrix, an apparent preferential location, particularly for the larger NPs, on the edges, ridges, or wrinkles of the graphitic carbon was observed. The average particle size and their distribution were determined by measuring a statistically relevant number of particles. The results appear, as listed in Table 1. This table shows that the mean diameter of the particles for samples **1** to **4** was slightly larger than 1 nm. This small average dimension of the Fe−Cu NPs is really remarkable, considering that the loading of these samples is above 10 wt % metal and in some cases close to 20 wt % and contrast with the larger mean diameters obtained by XRD (see Table 1). To understand a possible origin of this discrepancy between transmission electron microscopy (TEM) and XRD particle size, it should be reminded that XRD reports on the most crystalline, larger particles, whereas TEM can monitor all the particles, even those that contribute in the lesser extent to the XRD response.[19,20] As commented, when describing sample **5** derived from alginate and in contrast to samples **1** to **4** derived for chitosan as precursor, the average

particle size of Fe or Cu particles in sample **5** was about 100 nm, showing a core−shell structure (Figure 3i−k). Since the preparation of sample **5** was performed identically as those of samples **1** to **4**, it seems reasonable to attribute the much larger particle size for sample **5** to the absence of N doping of the resulting graphitic carbon matrix derived from alginate (no N-containing polysaccharide) as a precursor. Accordingly, the contrasting larger diameter of Fe−Cu NPs in sample **5** derived from alginate pyrolysis can be attributed to its high loading and the absence of the positive influence that the presence of nitrogen on the carbon matrix exerts on thwarting particle growth by providing strong interactions with the metal. Precedents in the literature have already observed the beneficial influence that nitrogen doping has on graphene and related carbons as supports to obtain small metal NPs.[21] As particle size is one of the major parameters influencing the catalytic activity of metal NPs, that undergo a significant decrease as the average dimension increases up to about 10 nm,[22,23] it can be foreseen that sample **5** should exhibit very low catalytic activity for the aqueous phase methanol reforming as it was in fact observed. Note that the core (Fe)−shell (Cu) structure of sample **5** cannot occur in samples **1** to **4** due to their much smaller particle size.

TEM of sample **5** having large particles revealed an inhomogeneous distribution of Fe and Cu, the former being predominantly located at the core and the latter at the shell. Energy-dispersive system (EDS) analysis along the particles shows this inhomogeneous location of the two metals [Figure 3 frames (i)−(k)]. Incidentally, it is worth noting that this core(Fe)−shell(Cu) structure clearly observed in sample **5** due to its large size would be compatible with having Cu and Fe in different phases, as indicated by XRD, while having a strong Fe−Cu interaction, as indicated by XPS. Additionally, this Fe−Cu interaction is required to interpret H_2-temperature-programmed reduction (TPR) measurements and the catalytic activity data.

To gain more information about the possible Fe−Cu interaction, H_2-TPR measurements of samples **1**, **2**, and **3** were carried out. It was expected that the reducibility of the single metal, either Cu in sample **1** or Fe in sample **2**, would be different when the two metals Cu and Fe are present in the material if an interaction between them exist. The H_2-TPR profiles are presented in Figure 4. As it can be seen there,
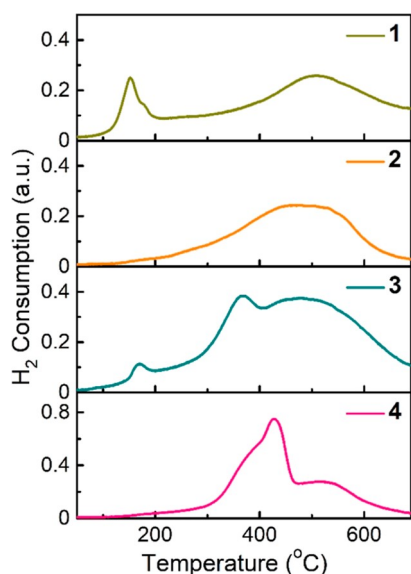
Figure 4. H_2-TPR plots of samples **1−4**.

monometallic Cu in sample **1** presents a reduction peak at about 175 °C that could be attributed to the reduction from Cu^{2+} to metallic Cu^+, followed by a further reduction to Cu^0 at about 500 °C. In comparison, monometallic Fe in sample **2** has a reduction peak by H_2 at 450 °C that should correspond to the reduction of Fe^{3+} present in the material to Fe^{2+}. These two peaks are also present in sample **3** that in addition exhibits a new reduction peak at an intermediate temperature of 375 °C that is proposed to arise from the Fe−Cu interaction. This specific peak would indicate that either Cu^{2+} ions are less easy to reduce or that Fe is more prone to undergo reduction. This interaction is further supported by the difference in the H_2-TPR profiles for samples **3** and **4**, with respect to samples containing only Cu (sample **1**) or only Fe (sample **2**), due to the different contents and proportions of Cu and Fe (Table 1). The difference in the profiles of samples **3** and **4** should be due to the different Cu/Fe ratios, with much lower Cu proportion in the case of sample **4**, as it is indicated in Table 1. Similar use of H_2-TPR to determine the interaction of Cu with other metals have been reported in the literature.[24,25]

■ CATALYTIC ACTIVITY

Catalytic experiments were carried out in a stainless-steel autoclave dissolving CH_3OH in the liquid H_2O phase in a CH_3OH/H_2O ratio of 1, corresponding to the stoichiometry of the CH_3OH reforming. This experimental detail will become relevant later when comparing the results obtained here for samples **1−4** with literature data. Preliminary studies in the absence of any catalyst or using a control of N-doped graphitic carbon without any metal show negligible H_2 evolution in the range of temperatures from 170 to 190 °C. In the literature, the catalytic activity of N-doped graphitic for aqueous phase reforming has been reported but adding significantly much larger amounts than those used in the present study,[26] thus showing that the Cu/Fe are the active sites in the present samples **1−5**. In contrast, in the presence of samples **1** to **4**, evolution of H_2, CO_2, accompanied by some minor CH_4 concentrations, was observed by analysis of the head space. Analysis of the liquid phase and the catalyst after the reaction by ^1H NMR spectroscopy does not detect the presence of methanol, formaldehyde, or formic acid.

Of note is that the amount of CO_2 in most of the experiments was lower than expected based on the stoichiometry of the reaction (Scheme 1). This less-than-expected CO_2 formation can be justified by the partial CO_2 dissolution−adsorption of this acid gas on the remaining aqueous phase and the catalyst during the course of the reaction as it has been previously proposed.[27,28] This defective amount of CO_2 in the gas phase does not allow to close the carbon balance of the reaction, however, as indicated above, the presence of organic compounds in the solid and aqueous phase was not detected by ^1H NMR spectroscopy.

On the other hand, CH_4 appears as a secondary product since it was only observed in those cases, in which the amount of H_2 and CO_2 was high. Generation of CH_4 has also been frequently observed in the aqueous phase methanol reforming.[29,30] It is proposed that CH_4 is formed from the Sabatier methanation of CO_2 promoted by the bimetallic catalyst. In the present case, this proposal is somewhat supported by the reported methanation activity of Fe alloys wrapped on graphitic carbon, although the reaction was performed in the gas phase, under continuous flow and higher temperature.

Worth commenting is the absence of detectable amounts of CO accompanying evolved H_2. CO is a strong poison of Pt and other noble metal catalysts generally employed in most of the
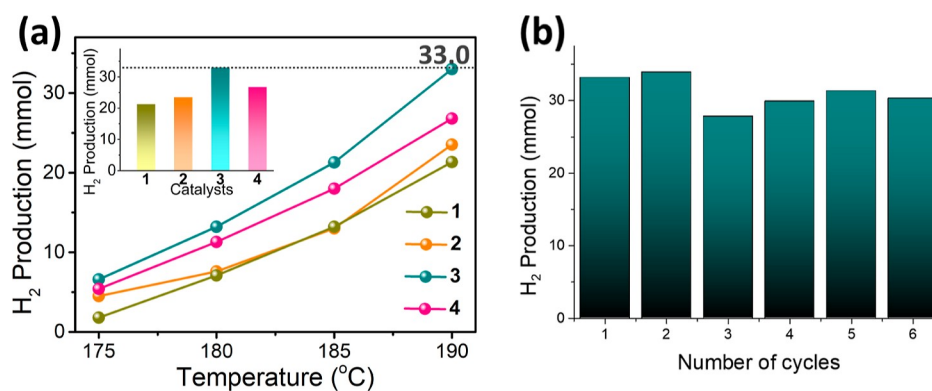

Figure 5. H_2 production for samples **1−4** under study. (a) H_2 evolution observed after 6 h reaction time as a function of the reaction temperature. Insert: H_2 production for each catalyst at 190 °C, (b) H_2 production for sample **3** in five consecutive reuses. Reaction conditions: catalyst 10 mg, methanol 460 μL (15 mmol), H_2O 280 μL (15 mmol), and reactor volume 15 mL.

potential applications of H_2 as an energy vector, such as the use in fuel cells.[31,32] Therefore, the absence of CO is a positive, wanted feature of the catalytic process promoted by the Fe−Cu catalysts.

Figure 5 presents the amount of H_2 observed after 6 h reaction time as a function of the temperature for the series of Fe−Cu catalysts under study. Table S3 provides complementary data on the amounts of CO_2 and CH_4 at final reaction time for the experiments, as shown in Figure 5. As it can be seen in this Figure 5, H_2 formation from aqueous phase CH_3OH reforming follows the order: **3 > 4 > 2 > 1 > 5**, at all the temperatures studied. Note that the surface area of the materials is mainly due to the graphitic carbon matrix that is the same for samples **1−4**. In comparison, the support of sample **5** is a graphitic carbon lacking N doping, and the core (Fe)−shell (Cu) particles have a much larger size than those of samples **1** to **4**. Although with somewhat lesser activity than the Fe−Cu combinations, it is notable that sample **2** containing exclusively Fe performs similarly and even better than sample **1** containing only Cu. This activity of the Fe NPs to promote aqueous phase methanol reforming is unprecedented. These results indicate the better performance of Fe−Cu combinations and the existence of an optimal Fe−Cu atomic ratio to achieve the highest H_2 evolution. For the best-performing sample **3** as a catalyst, a turnover frequency (TOF) value of 317 h^{-1} was estimated at full methanol conversion by dividing the number of initial methanol mols by the final time and the number of mols of metals in the catalyst, counting all the metal atoms as possible active centers for the aqueous phase reforming. This TOF value is similar to that reported for a highly active homogeneous Ru complex that requires the presence of hexanethiol to achieve high activity.[33]

In accordance with the favorable thermodynamics of the process, the amount of CH_3OH remaining in the reaction mixture after 6 h was low and undetectable for the experiment carried out at 190 °C in the presence of catalyst **3** after 6 h reaction time (see Table S3) for which CH_3OH conversion was complete.

Catalyst stability and deactivation were addressed by performing a series of six consecutive uses of the same sample. After each use, additional amounts of CH_3OH and H_2O were added into the autoclave before the subsequent reaction, keeping the solid catalyst inside the autoclave without any treatment. The results are also presented in Figure 5. As it can be seen there, the final H_2 production at 6 h remained basically unchanged with a production of 33 mmol of H_2 in the first use to a value of 29 mmol of H_2 in the sixth use.

Catalyst stability was also confirmed by characterization of the five times used sample by XRD, XPS, and TEM analyses. No change in the XRD (Figure 1) or XPS (Figure S4) of the five times used sample respect to the fresh material was observed, while a small particle size increase from the initial 1.1 nm average to a value of 1.3 nm after five consecutive uses was estimated from DF-TEM images (Figure S5).

To put the catalytic data achieved for sample **3** in a broader context, a literature survey was performed. The results are presented in Table S4. The figures of merit in the comparison are the TOF values and the reaction conditions. As can be seen in this Table S4, sample **3** based on Fe−Cu performs similarly but better than Pt or Ru catalysts. The performance of catalyst **3** is, on the other hand, significantly better than Ni containing catalysts. One important advantage of sample **3** is that no CO is detectable in the reformate gases, while this unwanted CO

gas has been generally observed in most of the reported catalysts, in some cases in very large amounts.

A final comment is that in most of the prior catalytic studies, an excess of methanol with respect to the amount of H_2O is used to achieve high TOF values. A general trend in the literature is that the TOF value increases with the excess of CH_3OH, a CH_3OH/H_2O molar ratio of 10 being not uncommon. In our case, the CH_3OH/H_2O molar ratio was maintained to the stoichiometric value of 1 (see Scheme 1), ensuring that there is not an excessive amount of the most valuable CH_3OH.

■ CONCLUSIONS

The present study has shown that, surprisingly, in view of the current compositions reported so far, earth-abundant Fe is a metal exhibiting catalytic activity for aqueous phase CH_3OH reforming and increases the catalytic activity of Cu. Although XRD indicates that the NPs do not correspond to a real random alloy of the two metals that are present in independent phases, there are evidences based on XPS and H_2-TPR showing charge transfer between the two metals. The small particle size (about 1 nm) in spite of the high loading makes these Fe−Cu NPs embedded within N-doped graphitic carbon matrix highly active catalysts for the aqueous phase reforming of methanol with stoichiometric amounts of H_2O. Complete CH_3OH reforming can be performed at 190 °C with TOF values of 317 h^{-1} without formation of CO and exhibiting a notable stability upon reuse. These materials compare favorably with other based on Pt, Pd, or Ru reported in the literature under similar reaction conditions. Overall, the present study shows the excellent catalytic activity that can be achieved for metal NPs embedded in N-doped graphitic carbon matrices conveniently prepared by pyrolysis of natural polysaccharides.

■ ASSOCIATED CONTENT

ⓢ Supporting Information

The Supporting Information is available free of charge at https://pubs.acs.org/doi/10.1021/acsaem.2c01806.

> Preparation and characterization of the Cu−Fe@(N)G samples, procedure of the catalytic aqueous methanol reforming, amount of reagents used in the preparation of each sample, XPS data of fresh and used sample **3**, FESEM images, TPR-H_2 and complementary catalytic data of samples **1−4**, and performance of sample **4** in comparison with the current state of the art (PDF)

■ AUTHOR INFORMATION

Corresponding Authors

Ana Primo − *Instituto Universitario de Tecnología Química CSIC-UPV, Universitat Politècnica de València, 46022 València, Spain;* Email: aprimoar@itq.upv.es

Hermenegildo García − *Instituto Universitario de Tecnología Química CSIC-UPV, Universitat Politècnica de València, 46022 Valencia, Spain; Center of Excellence in Advanced Materials Research, King Abdulaziz University, 22254 Jeddah, Saudi Arabia;* ⓞ orcid.org/0000-0002-9664-493X; Email: hgarcia@qim.upv.es

Authors

Alberto García-Baldoví − *Instituto Universitario de Tecnología Química CSIC-UPV, Universitat Politècnica de València, 46022 Valencia, Spain*

Lu Peng − *Instituto Universitario de Tecnología Química CSIC-UPV, Universitat Politècnica de València, 46022 Valencia, Spain;* Present Address: Department of Colloid Chemistry, Max Planck Institute of Colloids and Interfaces, D-14476 Potsdam, Germany

Andrea Santiago-Portillo − *Instituto Universitario de Tecnología Química CSIC-UPV, Universitat Politècnica de València, 46022 Valencia, Spain*

Abdullah M. Asiri − *Center of Excellence in Advanced Materials Research, King Abdulaziz University, 22254 Jeddah, Saudi Arabia;* ◉ orcid.org/0000-0001-7905-3209

Complete contact information is available at:
https://pubs.acs.org/10.1021/acsaem.2c01806

Author Contributions

The manuscript was written through contributions of all authors. All authors have given approval to the final version of the manuscript. A.G.-B. and L.P. contributed equally.

Notes

The authors declare no competing financial interest.

■ REFERENCES

(1) Abdin, Z.; Zafaranloo, A.; Rafiee, A.; Mérida, W.; Lipiński, W.; Khalilpour, K. R. Hydrogen as an energy vector. *Renewable Sustainable Energy Rev.* **2020**, *120*, 109620.

(2) Züttel, A. Hydrogen storage methods. *Naturwissenschaften* **2004**, *91*, 157−172.

(3) Teichmann, D.; Arlt, W.; Wasserscheid, P.; Freymann, R. A future energy supply based on Liquid Organic Hydrogen Carriers (LOHC). *Energy Environ. Sci.* **2011**, *4*, 2767−2773.

(4) Preuster, P.; Papp, C.; Wasserscheid, P. Liquid organic hydrogen carriers (LOHCs): toward a hydrogen-free hydrogen economy. *Acc. Chem. Res.* **2017**, *50*, 74−85.

(5) Wang, H.; He, T.; Du, Y.; Wang, W.; Shen, Y.; Li, S.; Zhou, X.; Yang, F. Evolution of single nanobubbles through multi-state dynamics. *Chin. Chem. Lett.* **2020**, *31*, 2442−2446.

(6) Nielsen, M.; Alberico, E.; Baumann, W.; Drexler, H.-J.; Junge, H.; Gladiali, S.; Beller, M. Low-temperature aqueous-phase methanol dehydrogenation to hydrogen and carbon dioxide. *Nature* **2013**, *495*, 85−89.

(7) Yao, C.; Wang, L.; Liu, Y.; Wu, G.; Cao, Y.; Dai, W.; He, H.; Fan, K. Effect of preparation method on the hydrogen production from methanol steam reforming over binary Cu/ZrO₂ catalysts. *Appl. Catal., A* **2006**, *297*, 151−158.

(8) Kamat, P. V. Graphene-based nanoarchitectures. Anchoring semiconductor and metal nanoparticles on a two-dimensional carbon support. *J. Phys. Chem. Lett.* **2010**, *1*, 520−527.

(9) Wang, R.; Wang, X.; Li, X.; Pei, L.; Gu, X.; Zheng, Z. Facile one-step synthesis of porous graphene-like g-C₃N₄ rich in nitrogen vacancies for enhanced H₂ production from photocatalytic aqueous-phase reforming of methanol. *Int. J. Hydrogen Energy* **2021**, *46*, 197−208.

(10) Ranjekar, A. M.; Yadav, G. D. Steam reforming of methanol for hydrogen production: A critical analysis of catalysis, processes, and scope. *Ind. Eng. Chem.* **2021**, *60*, 89−113.

(11) Primo, A.; Forneli, A.; Corma, A.; García, H. From biomass wastes to highly efficient CO₂ adsorbents: graphitisation of chitosan and alginate biopolymers. *ChemSusChem* **2012**, *5*, 2207−2214.

(12) Valentin, R.; Molvinger, K.; Quignard, F. o.; Brunel, D. Supercritical CO₂ dried chitosan: an efficient intrinsic heterogeneous catalyst in fine chemistry. *New J. Chem.* **2003**, *27*, 1690−1692.

(13) Primo, A.; Sánchez, E.; Delgado, J. M.; García, H. High-yield production of N-doped graphitic platelets by aqueous exfoliation of pyrolyzed chitosan. *Carbon* **2014**, *68*, 777−783.

(14) Climent, M. J.; Corma, A.; Iborra, S. Converting carbohydrates to bulk chemicals and fine chemicals over heterogeneous catalysts. *Green Chem.* **2011**, *13*, 520−540.

(15) He, J.; Anouar, A.; Primo, A.; García, H. Quality improvement of few-layers defective graphene from biomass and application for H₂ generation. *Nanomaterials* **2019**, *9*, 895.

(16) Peng, L.; Jurca, B.; Primo, A.; Gordillo, A.; Parvulescu, V. I.; García, H. Co-Fe Clusters Supported on N-Doped Graphitic Carbon as Highly Selective Catalysts for Reverse Water Gas Shift Reaction. *ACS Sustainable Chem. Eng.* **2021**, *9*, 9264−9272.

(17) Jurca, B.; Peng, L.; Primo, A.; Gordillo, A.; Parvulescu, V. I.; García, H. Co-Fe Nanoparticles Wrapped on N-Doped Graphitic Carbons as Highly Selective CO₂ Methanation Catalysts. *ACS Appl. Mater. Interfaces* **2021**, *13*, 36976−36981.

(18) Primo, A.; Quignard, F. Chitosan as efficient porous support for dispersion of highly active gold nanoparticles: design of hybrid catalyst for carbon-carbon bond formation. *Chem. Commun.* **2010**, *46*, 5593−5595.

(19) Nores-Pondal, F. J.; Vilella, I. M. J.; Troiani, H.; Granada, M.; de Miguel, S. R.; Scelza, O. A.; Corti, H. R. Catalytic activity vs. size correlation in platinum catalysts of PEM fuel cells prepared on carbon black by different methods. *Int. J. Hydrogen Energy* **2009**, *34*, 8193−8203.

(20) Akbari, B.; Tavandashti, M. P.; Zandrahimi, M. Particle size characterization of nanoparticles-a practicalapproach. *Iran. J. Mater. Sci. Eng.* **2011**, *8*, 48−56.

(21) Shi, R.; Zhao, J.; Liu, S.; Sun, W.; Li, H.; Hao, P.; Li, Z.; Ren, J. Nitrogen-doped graphene supported copper catalysts for methanol oxidative carbonylation: Enhancement of catalytic activity and stability by nitrogen species. *Carbon* **2018**, *130*, 185−195.

(22) Cojocaru, B.; Neaţu, Ş.; Sacaliuc-Pârvulescu, E.; Lévy, F.; Pârvulescu, V. I.; Garcia, H. Influence of gold particle size on the photocatalytic activity for acetone oxidation of Au/TiO₂ catalysts prepared by dc-magnetron sputtering. *Appl. Catal., B* **2011**, *107*, 140−149.

(23) Maillard, F.; Schreier, S.; Hanzlik, M.; Savinova, E. R.; Weinkauf, S.; Stimming, U. Influence of particle agglomeration on the catalytic activity of carbon-supported Pt nanoparticles in CO monolayer oxidation. *Phys. Chem. Chem. Phys.* **2005**, *7*, 385−393.

(24) Robertson, S.; McNicol, B.; De Baas, J.; Kloet, S.; Jenkins, J. Determination of reducibility and identification of alloying in copper-nickel-on-silica catalysts by temperature-programmed reduction. *J. Catal.* **1975**, *37*, 424−431.

(25) Yen, H.; Seo, Y.; Kaliaguine, S.; Kleitz, F. Role of metal-support interactions, particle size, and metal-metal synergy in CuNi nano-catalysts for H₂ generation. *ACS Catal.* **2015**, *5*, 5505−5511.

(26) Esteve-Adell, I.; Crapart, B.; Primo, A.; Serp, P.; Garcia, H. Aqueous phase reforming of glycerol using doped graphenes as metal-free catalysts. *Green Chem.* **2017**, *19*, 3061−3068.

(27) Manfro, R. L.; Da Costa, A. F.; Ribeiro, N. F. P.; Souza, M. M. V. M. Hydrogen production by aqueous-phase reforming of glycerol over nickel catalysts supported on CeO₂. *Fuel Process. Technol.* **2011**, *92*, 330−335.

(28) Xie, J.; Su, D.; Yin, X.; Wu, C.; Zhu, J. Thermodynamic analysis of aqueous phase reforming of three model compounds in bio-oil for hydrogen production. *Int. J. Hydrogen Energy* **2011**, *36*, 15561−15572.

(29) Coronado, I.; Stekrova, M.; García Moreno, L.; Reinikainen, M.; Simell, P.; Karinen, R.; Lehtonen, J. Aqueous-phase reforming of methanol over nickel-based catalysts for hydrogen production. *Biomass Bioenergy* **2017**, *106*, 29−37.

(30) Stekrova, M.; Rinta-Paavola, A.; Karinen, R. Hydrogen production via aqueous-phase reforming of methanol over nickel modified Ce, Zr and La oxide supports. *Catal. Today* **2018**, *304*, 143–152.

(31) Oh, S. H.; Sinkevitch, R. M. Carbon monoxide removal from hydrogen-rich fuel cell feedstreams by selective catalytic oxidation. *J. Catal.* **1993**, *142*, 254–262.

(32) Liguras, D. K.; Kondarides, D. I.; Verykios, X. E. Production of hydrogen for fuel cells by steam reforming of ethanol over supported noble metal catalysts. *Appl. Catal., B* **2003**, *43*, 345–354.

(33) Luo, J.; Kar, S.; Rauch, M.; Montag, M.; Ben-David, Y.; Milstein, D. Efficient Base-Free Aqueous Reforming of Methanol Homogeneously Catalyzed by Ruthenium Exhibiting a Remarkable Acceleration by Added Catalytic Thiol. *J. Am. Chem. Soc.* **2021**, *143*, 17284–17291.